Journal of Materials Chemistry A

ROYAL SOCIETY OF CHEMISTRY

COMMUNICATION

View Article Online
View Journal | View Issue

Cite this: J. Mater. Chem. A, 2022, 10, 2228

Received 9th December 2021
Accepted 1st January 2022

DOI: 10.1039/d1ta10538h

rsc.li/materials-a

Visualizing local fast ionic conduction pathways in nanocrystalline lanthanum manganite by isotope exchange-atom probe tomography†

Francesco Chiabrera, ‡[ab] Federico Baiutti, ‡*[ac] David Diercks, [d] Andrea Cavallaro, [e] Ainara Aguadero, [eg] Alex Morata [a] and Albert Tarancón §*[af]

The call for material systems with enhanced mass transport properties is central in the development of next-generation fuel cells, batteries and solid state energy devices in general. While two-dimensional doping by artificial heterostructuring or nanoscaling has shown great potential for overcoming kinetic limitations of ion diffusion, the length scale of interface effects requires the development of advanced tools for capturing and quantifying local phenomena in greater detail. In the present paper, an in-depth study of grain boundary oxygen conduction in Sr-doped lanthanum manganite films is presented by means of novel isotope-exchange atom probe tomography. Local pathways for fast mass transport are directly mapped by two-dimensional reconstructions and line profiles of the oxygen isotope concentration. Accurate finite element modelling is employed to retrieve the local kinetic parameters, highlighting an enhancement of two orders of magnitude for both the diffusivity and surface exchange rate with respect to the bulk ($D^*_{gb} = 2.1 \times 10^{-14}$ cm^2 s^{-1} and $k^*_{gb} = 4.3 \times 10^{-10}$ cm s^{-1}, respectively, for grain boundaries at 550 °C). Co-acquired reconstruction of the cationic distribution reveals strong inhomogeneities (dopant de-mixing) across the grain boundaries and in the sub-surface region, leading to local Sr accumulation. The findings provide unequivocal quantitative assessment of fast grain boundary oxygen diffusion in lanthanum strontium manganite, giving further insights into local stoichiometry deviations and promoting isotope exchange-atom probe tomography as a powerful tool for the study of local interface effects with high resolution. Different models for the explanation of the phenomena are critically discussed on the basis of the experimental findings.

Introduction

The modification of the local chemistry *via* the introduction of an interface is a strategy with great potential for engineering the electrochemical properties of functional oxides beyond the state of the art (SoA).[1–3] In mixed ionic-electronic conductors (MIECs), which find application *e.g.* as oxygen reduction electrocatalysts in solid oxide cells as well as in gas separation membranes,[4,5] solid solution is conventionally applied for increasing the electronic and oxygen vacancy concentration for oxygen exchange and diffusion.[6] Such an approach is however inherently limited *e.g.* by dopant solubility, by the reduction of ionic mobility caused by lattice disorder and defect association and, in some cases, by the high enthalpy of oxygen vacancy formation.[7–9] Due to the resulting limited ionic conductivity, the technological application of MIEC materials (*e.g.* as fuel cell cathodes) is based on MIEC/oxygen conductive fluorites (doped ceria or zirconia) composites.[10–12] Enhancing the bulk conductivity of MIECs is therefore of primary importance for activating the bulk reaction and oxygen transport path and providing a potentially superior alternative to triple phase boundary-based SoA composites. Recent works have demonstrated a substantial enhancement of surface exchange rate and oxygen diffusivity, with respect to the bulk, for example at grain boundaries (GBs) of $La_{0.8}Sr_{0.2}MnO_3$ (LSM), a model interface-dominated MIEC.[13,14] The origin of such an effect remains

[a]Catalonia Institute for Energy Research (IREC), Jardins de Les Dones de Negre 1, 08930 Sant Adrià del Besòs, Barcelona, Spain. E-mail: fbaiutti@irec.cat; atarancon@irec.cat

[b]Department of Energy Conversion and Storage, Functional Oxides Group, Technical University of Denmark, Fysikvej, 310, 233 2800 Kgs. Lyngby, Denmark

[c]Department of Materials Chemistry, National Institute of Chemistry, Hajdrihova 19, Ljubljana SI-1000, Slovenia

[d]Department of Metallurgical and Materials Engineering, Colorado School of Mines, Golden, CO 80401, USA

[e]Department of Materials, Imperial College London, Prince Consort Road, London SW7 2BP, UK

[f]ICREA, 23 Passeig Lluís Companys, Barcelona 08010, Spain

[g]Instituto de Ciencia de Materiales de Madrid (ICMM-CSIC), Sor Juana Inés De la Cruz, 3, 28049, Madrid, Spain

† Electronic supplementary information (ESI) available. See DOI: 10.1039/d1ta10538h

‡ Equal contribution.

§ Albert Tarancón writes: the paper is dedicated to John Kilner who possesses an innate talent for ionics and people. John is always opening doors for everyone. Indeed, meeting him opened the front door to this community for me. I will be always grateful for this. The current work is probably an ultimate answer to years of discussion with him on the outstanding ionic conductivity of LSM thin films. I am sure he will enjoy it.

elusive: the enhancement was ascribed to oxygen vacancy segregation at the grain boundary core according to theoretical investigations by Polfus *et al.*[15] Very recently, however, Börgers *et al.* have investigated fast mass transport along LSM dislocations, highlighting the role of space-charge effects.[16] The authors have also demonstrated that local oxygen kinetics in LSM can be *ad hoc* tailored by modifying the bulk stoichiometry.[17] Similar local effects on oxygen kinetics were found for $La_{0.8}Sr_{0.2}Mn_{1-x}Co_xO_3$ (LSMC) and for doped lanthanum chromite.[18,19] Notably, GB diffusivity and surface exchange coefficient in Sr-substituted thin films of lanthanum chromite are remarkably larger (two and one orders of magnitude, respectively) than for LSM GBs.[20]

While these results point out the potential of interface engineering for tuning oxygen kinetics and transport, the study of local mass transport presents a critical issue due to the impossibility of capturing such nanoscale effects with sufficient spatial resolution. Information obtained from diffusion profiles acquired by SoA techniques based on isotope exchange depth profiling (IEDP) is averaged over large areas (typically hundreds of μm^2)[21] and no information on the local chemical composition is usually accessible. These limitations prevent a complete understanding of diffusion phenomena and cause a considerable uncertainty for the retrieval of the kinetic parameters.[22] Very recently, we have demonstrated how atom probe tomography (APT) is able to overcome such shortcomings by providing a 3D-resolved reconstruction of atomic positions with nm-resolution and isotopic sensitivity.[20] In our previous studies, isotope exchange of thin films under controlled conditions allowed a direct observation – and reliable quantification – of fast oxygen diffusion pathways at LSCr grain boundaries and LSM–ceria interfaces.[12,20] Independent work by Kaspar *et al.* recently presented a similar approach for the study of buried Fe_2O_3 interfaces, confirming the broad relevance of the isotope exchange APT (IE-APT) approach.[23]

In the present study, IE-APT was used for the first-time visualization – and direct quantification – of previously reported enhancement of local oxygen transport in interface-dominated LSM. Fully dense nanocrystalline thin films have been fabricated by pulsed laser deposition (PLD) for a subsequent *ex situ* exchange in an ^{18}O-enriched atmosphere at controlled temperature. Sample conical tips of the exchanged films have been analyzed by APT providing a precise 3D chemical mapping and a direct visualization of nm-wide fast diffusion oxygen pathways. The experimental oxygen isotope fraction profiles have been simulated by finite element modelling (FEM) for a precise and independent quantification of the oxygen kinetic parameters for bulk, GBs (self-diffusion coefficient, D^*, and effective surface exchange coefficient, k^*) and for the analysis of mass transport in sub-surface regions. Local cationic distribution, as retrieved by IE-APT, is correlated to the observed functionalities.

Results and discussion

Nanocrystalline LSM thin films were deposited on top of ceria-buffered Al_2O_3 (0001) substrates. Single-phase LSM with a columnar fully dense structure (average grain size of 27 ± 3 nm) was obtained after deposition (Fig. 1a and ESI Fig. 1†).[17] The films were first annealed at 550 °C in an ^{18}O-enriched atmosphere, allowing the tracer to diffuse into the layer, and then analyzed by APT for the measurement of the ^{18}O fraction. Fig. 1, panels b–d shows the results of the IE-APT analysis. A sketch of an exchanged APT tip containing a single grain is represented in Fig. 1b (vertical cross-section). 2D contour plots of the oxygen isotope fraction profiles, $f(^{18}O) = [^{18}O]/([^{18}O] + [^{16}O])$, have been obtained from the APT tip reconstruction by integrating 2.5 nm-wide rectangular regions of interest relative to the film free surface: (i) perpendicular (vertical out-of-plane – Fig. 1c, $Y = 0$ nm) and (ii) parallel (horizontal in-plane – Fig. 1d, $Z = 20$ nm). In the out-of-plane contour plot, one can clearly identify channels of higher oxygen isotope content (up to $f(^{18}O) \approx 7 \times 10^{-2}$), which correspond to narrow and fast conducting regions and which can be spatially correlated to the structurally

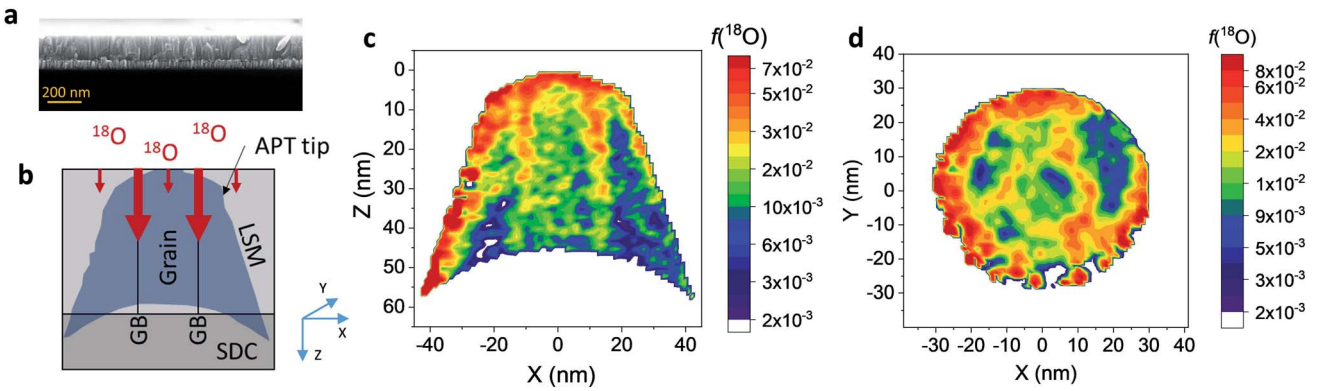

Fig. 1 (a) Cross-sectional SEM micrograph of LSM/SDC bilayer (reference sample on Si substrate) (b) sketch of the IE-APT measurement for nanocrystalline columnar LSM thin films (shadowed region corresponds to the LSM APT tip). IE-APT measurements of the (c) vertical and (d) horizontal cross sections of the ^{18}O fraction (color scale) in LSM thin films. The vertical cross section corresponds to $Y = 0$ nm while the horizontal cross section is taken at 20 nm from the free surface ($Z = 20$). ^{18}O fraction is reported in logarithmic scale to better visualize the difference in isotope concentration between grain interior and GBs.

observed GBs. The horizontal separation between such regions is ≈30 nm, consistent with the grain size as retrieved by AFM and cross-sectional SEM (Fig. 1a and ESI Fig. 1†). A detailed analysis of the oxygen tracer fraction for bulk and GBs is reported later in the text. The in-plane contour (Fig. 1d) highlights the columnar shape of the ^{18}O accumulation GBs as shown in Fig. 1a and elsewhere.[17] Note that the apparent ^{18}O accumulation at the lateral edge of the tip should be interpreted as an experimental artifact likely due to surface damage/contamination from the Ga focused ion beam preparation of the specimen. The region was confined to the edge of the analyzed specimen and it was observed to have high Ga, C, and H concentrations and greater overall background counts in the mass spectrum. The large field of view obtained from these specimens, which was not observed previously,[12,20] is tentatively assigned to the specific film–substrate combination and in particular to the very high evaporation field of the alumina substrate.[24]

FEM simulations have been employed in order to calculate the values of the oxygen transport parameters of LSM bulk and GB (k^* and D^*) by fitting the APT reconstruction profiles – Fig. 2. 2D model geometries were selected for accurately reproducing the out-of-plane IE-APT reconstructions (*cf.* Fig. 1a and ESI Fig. 2†), which present grain interior areas (characterized by D^*_g and k^*_g) separated by 1 nm-thick GBs (with kinetic parameters D^*_{gb} and k^*_{gb} – fast GB core).[18,20] An additional parameter ($D^*_{g,s}$) was introduced in the model for qualitatively describing the (slower) diffusion of the grain interior in the subsurface region, which accounts for the observed initial steep decrease of the tracer fraction for $Z < 5$ nm (Fig. 2b). This assumption is justified on the basis of strong cationic deviations measured by APT – *cf.* later in the text – and of previous reports *e.g.* on Fe-doped $SrTiO_3$, reporting slow subsurface oxygen diffusivity as a consequence of space-charge effects.[25] Please refer to ESI Notes 1 and 2† for details on the FEM modelling, including sensitivity analysis. Fig. 2b shows the 2D contour of the FEM model after fitting of the experimental data (Fig. 2a) by systematic parameterization. The optimized FEM model is able to accurately describe the IE-APT results (apart from very local inhomogeneities) yielding: (i) fast oxygen incorporation and diffusivity at the GB ($D^*_{gb} = 2.1 \times 10^{-14}$ cm^2 s^{-1}, $k^*_{gb} = 4.3 \times 10^{-10}$ cm s^{-1} at 550 °C); (ii) slower diffusivity and surface exchange rate for the bulk ($D^*_g = 1.0 \times 10^{-16}$ cm^2 s^{-1}, $k^*_g = 4.5 \times 10^{-12}$ cm s^{-1}); (iii) reduced sub-surface diffusivity ($D^*_{g,s} = 1.5 \times 10^{-17}$ cm^2 s^{-1} – note that the sub-surface region width is assumed as 5 nm – *cf.* later in the text).

Unlike conventional tracing methods based on secondary ion mass spectrometry (SIMS) – which offer only averaged data over hundreds of μm^2 – IE-APT allows extracting direct information on the local tracer fraction with nm-resolution in all directions (X–Y–Z). A segmented analysis of the data is therefore accessible for a separate study of the different sample areas as

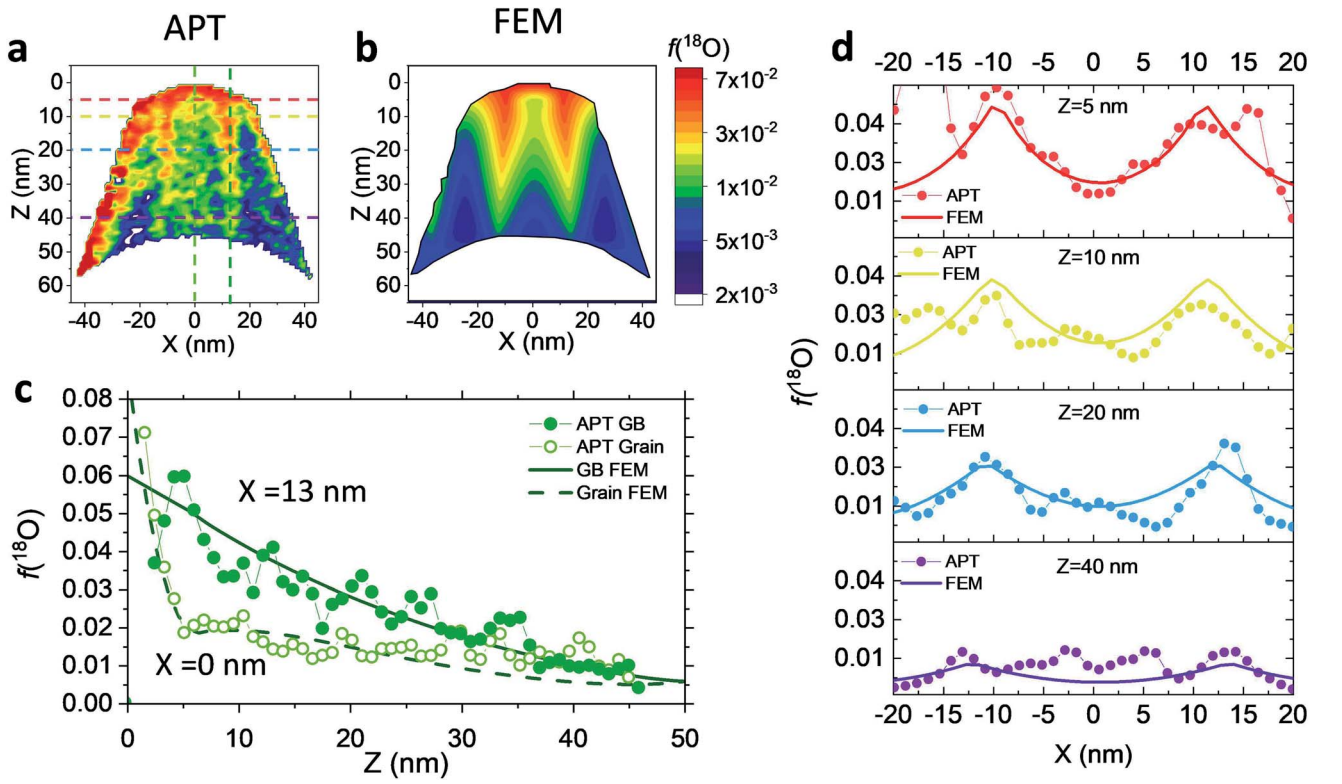

Fig. 2 2D vertical cross section of the ^{18}O fraction measured by APT (a) and obtained by FEM simulations (b). (c) 1D out-of-plane profiles of the isotope fraction obtained along a GB and along the grain bulk of the LSM tip, as measured by IE-APT and calculated in the FEM simulation. (d) 1D horizontal ^{18}O fraction measured at different distances from the sample's surface. The vertical and horizontal 1D profiles shown in (c) and (d) are depicted in a as dashed lines.

shown in Fig. 2c, in which light and dark green dotted lines correspond to 1D out-of-plane experimental profiles along bulk and a selected GB, respectively. In-plane 1D profiles of $f(^{18}O)$ are represented in Fig. 2d (profiles extracted along the dotted lines in Fig. 2a). Using these data, $f(^{18}O)$ for the two phases can be independently fit for a very precise quantification. The results highlight that isotopes incorporation in the bulk grain originates from lateral diffusion from the GBs ($D^*_g = 1.0 \times 10^{-16}$ cm^2 s^{-1}) giving rise to a concentration gradient in the X-direction (Fig. 2d). Conversely, vertical mass transport through the bulk is strongly suppressed. Finally, a local accumulation of oxygen isotope is confirmed in the sub-surface (*cf.* grain $f(^{18}O)$ profile in Fig. 2c, $Z < 5$ nm). This effect can be modelled by the introduction of the previously mentioned sub-surface diffusivity, $D^*_{g,s}$, which strongly improves the fitting of the bulk tracer profile (while the quality of the GBs modelling remain largely unaffected – please refer to ESI Fig. 3,† which includes two FEM fittings obtained for the same set of parameters, with and without $D^*_{g,s}$).

Effects stemming from trajectory aberration are known to limit the APT resolution to ≈2 nm at phase contacts, preventing a local study of the oxygen content in the grain boundary core.[26] In ESI Note 3,† we discuss an alternative FEM model based on the space-charge accumulation of oxygen vacancies (and strong reduction of oxygen diffusivity in the core). This behavior may originate from the segregation of the acceptor dopant (Sr'_{La}) or cationic vacancies (V'''_{La} or V'''_{Mn}) in the core, giving rise to a negatively charged interface and promoting the accumulation of positively charged oxygen vacancies in the GB surroundings. We note that, in bulk LSM under oxidizing conditions, the concertation of cationic vacancies and acceptor dopant Sr is high,[27] while oxygen vacancies, which are typically expected to segregate at the GB core in ionic conductors,[28] are a minority defect. This interesting scenario was recently proposed by Börgers *et al.* to explain fast diffusion along dislocation in LSM.[16] The result of the simulations (ESI Fig. 8†) show that also this model is able to adequately describe the $f(^{18}O)$ profiles.[15,16] Importantly, the resulting kinetic parameters are very close to the ones obtained by considering fast core diffusivity (Fig. 2).

The resulting k^* and D^* are compared to literature data (stoichiometric[13] and B-site deficient LSM[14]) in Fig. 3: the values (measured here for $T = 550$ °C) are well in line with previous literature reports, confirming the quality of our approach based on IE-APT. The observed enhancement of both k^*_{gb} and D^*_{gb} is about two orders of magnitude with respect to the bulk. $D^*_{g,s}$ is reduced by about one order of magnitude in comparison to D^*_g, yet within typical values for bulk LSM.

Fig. 4 shows independent 2D contour plots of the different ionic species (La, Mn, Sr and O in Fig. 4a–d, respectively) and linescans along horizontal ($Z = 20$ nm in Fig. 4f) and vertical directions ($X = 0$ in Fig. 4g). As a first general observation, important deviations from the nominal stoichiometry are present for A-site cations with Sr-content x ranging from ~0.10 to ~0.5 in $La_{1-x}Sr_xMnO_3$, within a length scale ≈10 nm. (Please note that some uncertainty in the absolute atomic concentration may be introduced by the APT technique).[12,30] Fig. 4a (La contour) also highlights a strong modulation of La concentration (especially in the proximity of the fast oxygen diffusion pathways), which is complementary to Sr (*cf.* also Fig. 4c and f). Although such a relation is predictable (Sr being an A-site substitutional dopant), such a very broad non-stoichiometry at the nanoscale level is unexpected. It is noteworthy that this uneven distribution of A-site cations does not involve variations in the Mn distribution map within the resolution of the technique (Fig. 4b), confirming a homogeneous presence of the ABO_3 perovskite phase (*cf.* also Fig. 1). Intriguingly, the variation of the A-site distribution is different for each GB (labelled as GB_1 and GB_2) and clear compositional differences can be observed between the two GBs. This is particularly clear in the 1D profiles shown in Fig. 4e (crossing GB_1 and GB_2). Namely, GB_1 is characterized by a strong

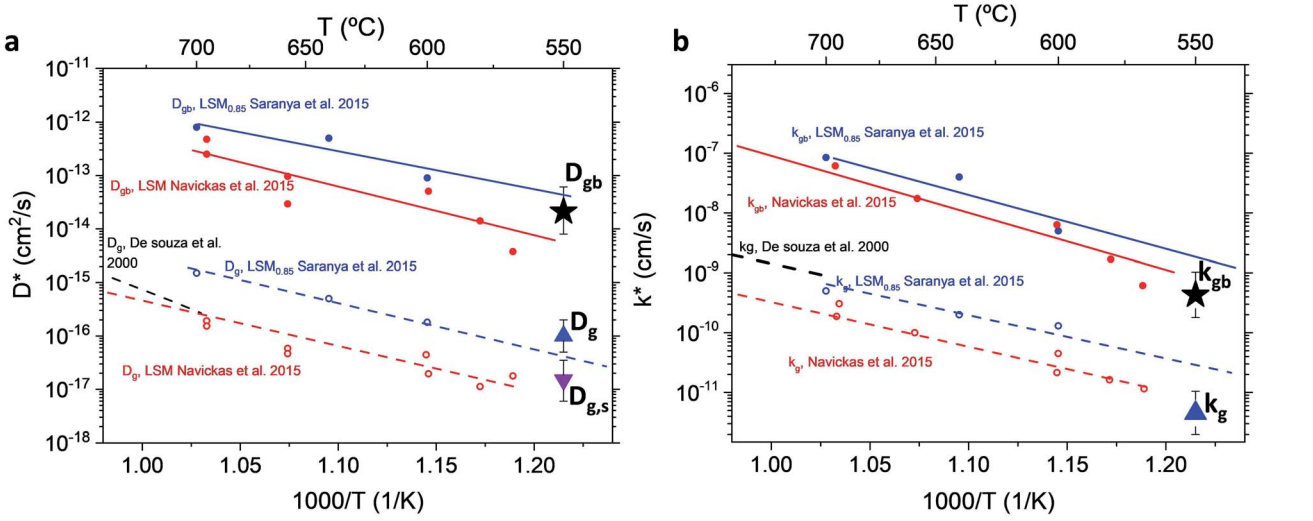

Fig. 3 Diffusivity (a) and surface exchange coefficient (b) for nanocrystalline LSM measured by APT and compared to literature values (for stoichiometric and B-site deficient ($LSM_{0.85}$) materials).[13,14,29] Values from Saranya *et al.* 2015 (ref. 14) have been updated using the FEM model introduced by the authors in Saranya *et al.* 2018 (ref. 18). The error bars are calculated from the sensitivity analysis described in ESI Note 2.†

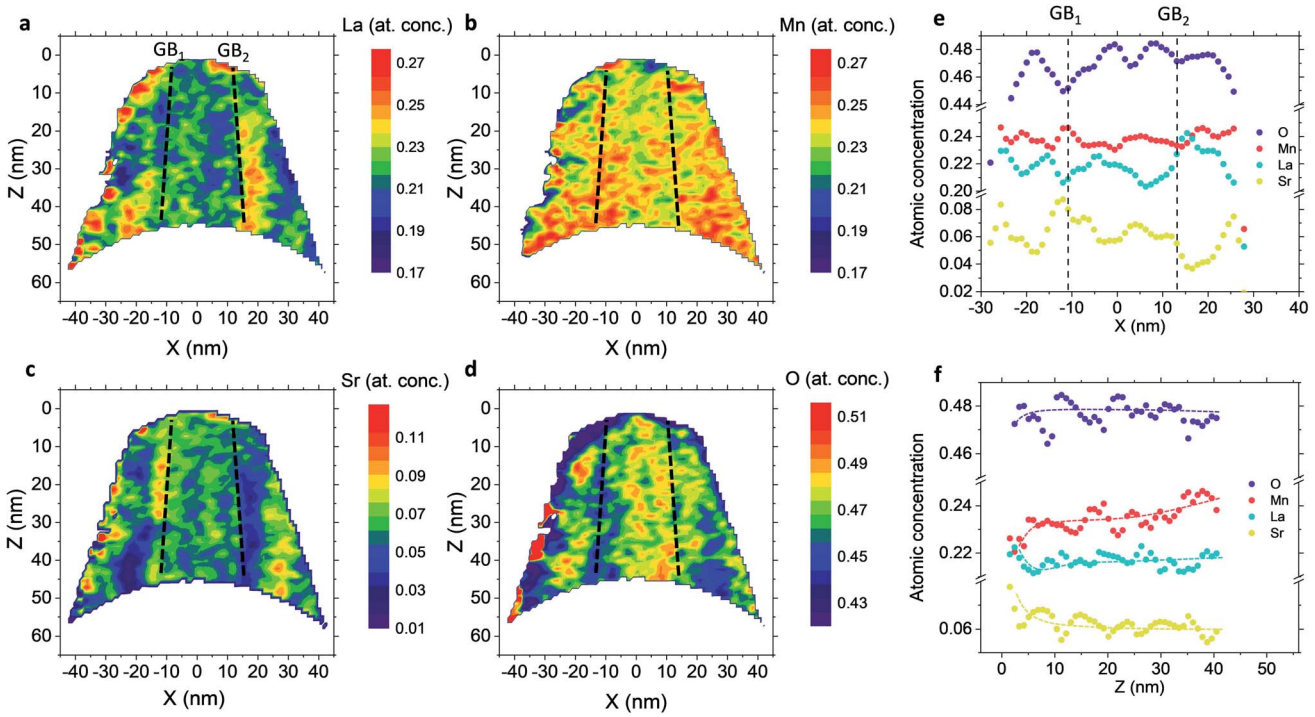

Fig. 4 Vertical cross-section contour plots of the atomic concentration for La (a), Mn (b), Sr (c) and O (d) measured by ATP. The position of the GBs is highlighted in the figures by black dashed lines, labelling the two GBs present as GB_1 and GB_2. (e) Horizontal linescan profiles of the elemental concentration of the atomic species crossing two GBs (referred as vertical dashed black lines). Linescan profiles are taken at $Z = 20$ nm. (f) Vertical linescan profiles of the atomic concentration of the species in the grain interior ($X = 0$), showing an A-site enrichment in the first 5 nm. The dotted lines are a guide for the eye.

Sr accumulation (up to $x \sim 0.5$) that is not observed for GB_2 (which is closer to stoichiometry). In both cases, Sr depletion occurs especially on one side of the boundary. As far as the total oxygen content is concerned ($^{18}O + {}^{16}O$), a clear depletion is found in correspondence to the high Sr concentration areas (Fig. 4d), in agreement with a classical electroneutral situation ($2[V_O^{\cdot\cdot}] + h^{\cdot} = [Sr'_{La}]$).[31] Oxygen diffusivity, however, seems not to be directly related to such strong compositional variations, as similar kinetic parameters characterize GB_1 and GB_2 (*cf.* Fig. 1). We ascribe such an apparent discrepancy to the different lengths scales under consideration (≈10 nm for the observed stoichiometry changes *vs.* <3 nm for fast-conducting GB width),[16,17] alongside possible mobility effects. Note that the observed strong dopant segregation is expected to have a stronger impact on the electronic conductivity and magnetic properties of LSM.[32–34] Overall, such findings (and similar observations previously reported by our group for nanocrystalline lanthanum chromite)[20] call attention to the need of accurate models which capture the different driving forces for a proper description of local chemistry and relevant cation non-stoichiometry in non-dilute systems. A Poisson–Cahn approach, accounting for the electrostatic, but also structural and elastic contributions in non-diluted system, could in principle provide the rationale for the observed ion accumulation at the grain boundaries.[16,35,36] Improved models will be of utmost importance to understand and qualify the recently reported tendency of dopant de-mixing in MIEC materials.[37]

Lastly, the out-of-plane ionic profiles are analyzed in Fig. 4f (grain interior). A progressive decrease of the Mn content towards the free surface of the film ($Z = 0$) is highlighted, alongside a very strong accumulation of Sr and La in the sub-surface region ($Z < 10$ nm).[38,39] Notably, the thickness of such a region, characterized by different stoichiometry, corresponds to the oxygen isotope accumulation area highlighted in Fig. 1 and can therefore be tentatively accounted for the local low $D^*_{g,s}$ described previously. Note also that APT is able to retrieve local information on single grains and is therefore in principle unaffected by intergranular porosity/roughness for the assessment of the surface region.

Conclusion

A complete description of local oxygen mass transport properties for nanocrystalline LSM is reported by a novel approach consisting on isotope exchange depth profiling combined with atom probe tomography. The analysis provides the first direct visualization of the recently reported fast grain boundary oxygen diffusion in LSM, with nm-resolution in all directions. Experimental data include cationic and oxygen two-dimensional distribution maps and have been fit, for the case of isotopic oxygen, by an accurate finite element modelling of the microstructure. FEM, provided with an accurate independent quantification of oxygen mass transport properties for LSM at the bulk and grain boundary levels, revealed values of

$D^*_{gb} = 2.1 \times 10^{-14}$ cm^2 s^{-1} and $k^*_{gb} = 4.3 \times 10^{-10}$ cm s^{-1} at 550 °C for grain boundary diffusivity and surface exchange coefficient, respectively. These are in good agreement with previous figures obtained by conventional averaging techniques such as IEDP-SIMS. Local compositional maps of cationic distributions disclosed the presence of remarkable inhomogeneities in the Sr-dopant content (ranging from $x = 0.1$ to $x = 0.5$ in only few tens of nanometers), uniform Mn distribution and the presence of an A site-enriched subsurface region. The combined (and overlapping) quantification of cation, oxygen and isotope distributions allowed by IE-APT will likely become a common tool in the near future, giving rise to relevant data that will help developing robust models for explaining oxygen diffusion at the nanoscale or other relevant diffusive phenomena such as de-mixing effects in MIEC perovskites, which may strongly impact multiple applications like electrocatalysis, electrochemistry or magnetism.

Experimental section

Films fabrication

LSM thin films were deposited by large-area PLD (PVD Systems – PLD 5000) using a 248 nm KrF excimer laser (Lambda Physics – COMPex PRO 205). The layers were deposited on Al_2O_3 (0001) single crystal substrate (Crystec GmbH). A thin barrier layer of $Ce_{0.8}Sm_{0.2}O_{1.9}$ (SDC) was deposited before the LSM film in order to avoid cationic intermixing at the interface.[40] Both layers were deposited at 700 °C, under an oxygen pressure of 2.6×10^{-2} mbar, target–substrate distance of 95 mm, laser fluency ≈1.2 J cm^{-2} and 5 Hz of laser frequency. The thickness of LSM and SDC layers deposited was ≈45 nm and ≈35 nm, respectively, as measured by spectroscopy ellipsometry (UVISEL, Horiba scientific).

Structural characterization

X-ray diffraction was carried out using a Bruker D8 Advance diffractometer with a Cu K_α radiation source in a $2\theta/\omega$ configuration (1.5° offset), step size 0.01° and counting time 1 s per step. Atomic force microscopy was carried out in a Park System and analyzed by Gwyddion software. Scanning electron microscopy was carried out on a Zeiss Auriga Equipment (InLens detector).

Oxygen exchange

After cleaning the LSM thin film sample surfaces by pure ethanol and acetone, an annealing in 200 mbar of pure oxygen N5 (99.999%) with $^{18}O_2$ in the normal isotopic abundance was performed. Once the samples were cooled down at room temperature, the exchanged tube was evacuated and filled with an ~90% $^{18}O_2$ enriched gas (200 mbar). Following the exchange, the samples were quenched to room temperature. The nominal exchange temperature and time were 550 °C and 1 h and 40 min, respectively.

Atom probe tomography

Atom probe tomography (APT) specimens were prepared using a lift-out technique in an FEI Helios NanoLab 600i focused ion beam/scanning electron microscope (FIB/SEM). Specimens were mounted on TEM grids and hardware that allowed for TEM imaging (FEI Talos F200X) and analysis of the APT specimens.[41] Initial shaping was performed using a 30 kV Ga^+ ion beam voltage, with 2 kV used for final sharpening.

APT (Cameca LEAP 4000X Si) was performed at 45.5 K using a 30 pJ laser energy and 500 kHz pulse rate. The flight path length was 90 mm and the ion detection rate was set to 5 ions per 1000 pulses, resulting in a bias range of 5000–7400 V during the data collection. Reconstructions were generated in Cameca's IVAS 3.6.18 software using the TEM images of the specimens before and after APT analysis (ESI Fig. 9†) for setting the reconstruction parameters.[42] A systematic energy deficit correction was employed to improve the mass spectral resolution.[43]

Finite element modelling

FEM simulations were performed by COMSOL Multiphysics to model the heterogeneous ^{18}O incorporation and diffusion in the LSM thin films. The 2D geometry was modelled directly on the vertical cross section obtained by the IE-APT measurement (*cf.* Fig. 1 and ESI Notes 2 and 3†). Two different diffusivity coefficients were considered for bulk and GB regions (D^*_b and D^*_{gb}). The width of the GBs was fixed to 1 nm, in accordance with previous works.[13,18,20] Oxygen incorporation was modelled by a convective-type boundary condition, employing two different surface exchange parameters for bulk and GB surfaces (k^*_b and k^*_{gb}). To reproduce the steep decrease of tracer observed in the bulk subsurface, a different diffusivity coefficient was considered in the first 5 nm ($D^*_{b,s}$). Fick's second law of diffusion was then solved by FEM method. The 2D results of the ^{18}O fraction obtained by the simulations were cut with the shape of the APT tip in order to offer a more direct comparison with the experimental data. Details on the FEM simulations including sensitivity analysis can be found in ESI Notes 1 and 2† and in our previous works.[18,20]

Conflicts of interest

There are no conflicts of interest to declare.

Acknowledgements

This project received funding from the European Union's Horizon 2020 research and innovation program under grant agreement No. 824072 (HARVESTORE) and No. 101017709 (EPISTORE) and under the Marie Skłodowska-Curie grant agreement No. 840787 (Thin-CATALYzER).

References

1 P. Lupetin, G. Gregori and J. Maier, *Angew. Chem., Int. Ed.*, 2010, **49**, 10123–10126.
2 F. Gunkel, D. V. Christensen and N. Pryds, *J. Mater. Chem. C*, 2020, **8**, 11354–11359.

3 M. D. Armstrong, K. W. Lan, Y. Guo and N. H. Perry, *ACS Nano*, 2021, **15**, 9211–9221.
4 B. Wang, J. Yi, L. Winnubst and C. Chen, *J. Membr. Sci.*, 2006, **286**, 22–25.
5 E. D. Wachsman and K. T. Lee, *Science*, 2011, **334**, 935–939.
6 R. A. De Souza and J. Kilner, *Solid State Ionics*, 1999, **126**, 153–161.
7 W. Jung and H. L. Tuller, *Energy Environ. Sci.*, 2012, **5**, 5370–5378.
8 J. Koettgen, S. Grieshammer, P. Hein, B. O. H. Grope, M. Nakayama and M. Martin, *Phys. Chem. Chem. Phys.*, 2018, **20**, 14291–14321.
9 D. S. Mebane, Y. Liu and M. Liu, *Solid State Ionics*, 2008, **178**, 1950–1957.
10 V. Dusastre and J. A. Kilner, *Solid State Ionics*, 1999, **126**, 163–174.
11 S. Anelli, F. Baiutti, A. Hornés, L. Bernadet, M. Torrell and A. Tarancón, *J. Mater. Chem. A*, 2019, **7**, 27458–27468.
12 F. Baiutti, F. Chiabrera, M. Acosta, D. Diercks, D. Parfitt, J. Santiso, X. Wang, A. Cavallaro, A. Morata, H. Wang, A. Chroneos, J. MacManus-Driscoll and A. Tarancon, *Nat. Commun.*, 2021, **12**, 1–11.
13 E. Navickas, T. M. Huber, Y. Chen, W. Hetaba, G. Holzlechner, G. Rupp, M. Stöger-Pollach, G. Friedbacher, H. Hutter, B. Yildiz and J. Fleig, *Phys. Chem. Chem. Phys.*, 2015, **17**, 7659–7669.
14 A. M. Saranya, D. Pla, A. Morata, A. Cavallaro, J. Canales-Vázquez, J. A. Kilner, M. Burriel and A. Tarancõn, *Adv. Energy Mater.*, 2015, **5**, 1500377.
15 J. M. Polfus, B. Yildiz and H. L. Tuller, *Phys. Chem. Chem. Phys.*, 2018, **20**, 19142–19150.
16 J. M. Börgers, J. Kler, K. Ran, E. Larenz, T. E. Weirich, R. Dittmann and R. A. De Souza, *Adv. Funct. Mater.*, 2021, **2105647**, 1–8.
17 F. Chiabrera, I. Garbayo, L. López-Conesa, G. Martín, A. Ruiz-Caridad, M. Walls, L. Ruiz-González, A. Kordatos, M. Núñez, A. Morata, S. Estradé, A. Chroneos, F. Peiró and A. Tarancón, *Adv. Mater.*, 2019, **31**, 1805360.
18 A. M. A. M. Saranya, A. Morata, D. Pla, M. Burriel, F. Chiabrera, I. Garbayo, A. Hornés, J. A. J. A. Kilner and A. Tarancón, *Chem. Mater.*, 2018, **30**, 5621–5629.
19 I. Yasuda, *J. Electrochem. Soc.*, 1994, **141**, 1268.
20 F. Baiutti, F. Chiabrera, D. Diercks, A. Cavallaro, L. Yedra, L. López-Conesa, S. Estradé, F. Peiró, A. Morata, A. Aguadero and A. Tarancón, *Adv. Mater.*, 2021, **33**, 2105622.
21 R. A. De Souza, J. Zehnpfenning, M. Martin and J. Maier, *Solid State Ionics*, 2005, **176**, 1465–1471.
22 J. M. Börgers and R. A. De Souza, *Phys. Chem. Chem. Phys.*, 2020, **22**, 14329.
23 T. C. Kaspar, S. D. Taylor, K. H. Yano, T. G. Lach, Y. Zhou, Z. Zhu, A. A. Kohnert, E. K. Still, P. Hosemann, S. R. Spurgeon and D. K. Schreiber, *Adv. Mater. Interfaces*, 2021, **8**, 2001768.
24 F. Vurpillot, D. Larson and A. Cerezo, *Surf. Interface Anal.*, 2004, **36**, 552–558.
25 R. A. De Souza and M. Martin, *Phys. Chem. Chem. Phys.*, 2008, **10**, 2356–2367.
26 F. Vurpillot, A. Bostel and D. Blavette, *Appl. Phys. Lett.*, 2000, **76**, 3127–3129.
27 F. Poulsen, *Solid State Ionics*, 2000, **129**, 145–162.
28 R. A. De Souza, *Phys. Chem. Chem. Phys.*, 2009, **11**, 9939–9969.
29 R. A. De Souza, J. A. Kilner and J. F. Walker, *Mater. Lett.*, 2000, **43**, 43–52.
30 R. J. H. Morris, M. Popovici, J. Meersschaut, J. Scheerder, L. Goux, G. Kar, C. Fleischmann, W. Vandervorst and P. van der Heide, *Microsc. Microanal.*, 2021, **27**, 2480–2481.
31 F. Kröger and H. Vink, *Solid State Phys.*, 1956, **3**, 307–435.
32 L. Malavasi, *J. Mater. Chem.*, 2008, **18**, 3295.
33 F. Chiabrera, I. Garbayo, D. Pla, M. Burriel, F. Wilhelm, A. Rogalev, M. Núñez, A. Morata and A. Tarancón, *APL Mater.*, 2019, **7**, 013205.
34 A. Urushibara, Y. Moritomo, T. Arima, A. Asamitsu, G. Kido and Y. Tokura, *Phys. Rev. B: Condens. Matter Mater. Phys.*, 1995, **51**, 14103–14109.
35 D. S. Mebane and R. A. De Souza, *Energy Environ. Sci.*, 2015, **8**, 2935–2940.
36 K. S. N. Vikrant, W. C. Chueh and R. E. García, *Energy Environ. Sci.*, 2018, 1993–2000.
37 M. A. R. Niania, A. K. Rossall, J. A. V. den Berg and J. A. Kilner, *J. Mater. Chem. A*, 2020, **8**, 19414–19424.
38 Z. Cai, M. Kubicek, J. Fleig and B. Yildiz, *Chem. Mater.*, 2012, **24**, 1116–1127.
39 M. A. R. Niania, A. K. Rossall, J. A. Van Den Berg and J. A. Kilner, *J. Mater. Chem. A*, 2020, **8**, 19414–19424.
40 B. Kamecki, J. Karczewski, H. Abdoli, M. Chen, G. Jasiński, P. Jasiński and S. Molin, *J. Electron. Mater.*, 2019, **48**, 5428–5441.
41 B. P. Gorman, D. Diercks, N. Salmon, E. Stach, G. Amador and C. Hartfield, *Microsc. Today*, 2008, **16**, 42–47.
42 D. R. Diercks and B. P. Gorman, *Ultramicroscopy*, 2018, **195**, 32–46.
43 B. W. Caplins, P. T. Blanchard, A. N. Chiaramonti, D. R. Diercks, L. Miaja-Avila and N. A. Sanford, *Ultramicroscopy*, 2020, **213**, 112995.

